Title

Novel window for cancer nanotheranostics: non-invasive ocular assessments of tumor growth and nanotherapeutic treatment efficacy in vivo.

Journal

Biomedical Optics Express, 10(1)

ISSN

2156-7085

Authors

Goswami, Mayank
Wang, Xinlei
Zhang, Pengfei
et al.

Publication Date

2019

DOI

10.1364/boe.10.000151

Peer reviewed

Research Article | Vol. 10, No. 1 | 1 Jan 2019 | BIOMEDICAL OPTICS EXPRESS 151
Biomedical Optics EXPRESS

Novel window for cancer nanotheranostics: non-invasive ocular assessments of tumor growth and nanotherapeutic treatment efficacy *in vivo*

MAYANK GOSWAMI,[1,2] XINLEI WANG,[3] PENGFEI ZHANG,[1] WENWU XIAO,[4] SARAH J. KARLEN,[3] YUANPEI LI,[4] ROBERT J. ZAWADZKI,[1,5] MARIE E. BURNS,[3] KIT S. LAM,[4,7] AND EDWARD N. PUGH JR[1,3,6,8]

[1]*EyePod Small Animal Ocular Imaging Laboratory, University of California, Davis, CA 95616, USA*
[2]*Currently with Department of Physics, Indian Institute of Technology Roorkee, Roorkee, 247667, India*
[3]*Department of Cell Biology and Human Anatomy, University of California, Davis, CA 95616, USA*
[4]*Department of Biochemistry and Molecular Medicine and Comprehensive Cancer Center, University of California, Davis, Sacramento, CA 95817, USA*
[5]*Vision Science and Advanced Retinal Imaging Laboratory (VSRI) Department of Ophthalmology and Vision Science, University of California, Davis, CA 95616, USA*
[6]*Department of Physiology and Membrane Biology, University of California, Davis, CA 95616, USA*
[7]*kslam@ucdavis.edu*
[8]*enpugh@ucdavis.edu*

Abstract: In cancer research there is a fundamental need for animal models that allow the *in vivo* longitudinal visualization and quantification of tumor development, nanotherapeutic delivery, the tumor microenvironment including blood vessels, macrophages, fibroblasts, immune cells, and extracellular matrix, and the tissue response to treatment. To address this need, we developed a novel mouse ocular xenograft model. Green fluorescent protein (GFP) expressing human glioblastoma cells (between 500 and 10,000) were implanted into the subretinal space of immunodeficient mice (56 eyes). The resultant xenografts were imaged *in vivo* non-invasively with combined fluorescence scanning laser ophthalmoscopy (SLO) and volumetric optical coherence tomography (OCT) for a period up to several months. Most xenografts exhibited a latent phase followed by a stable or rapidly increasing volume, but about 1/3 underwent spontaneous remission. After prescribed growth, a population of tumors was treated with intravenously delivered doxorubicin-containing porphyrin and cholic acid-based nanoparticles ("nanodox"). Fluorescence resonance energy transfer (FRET) emission (doxorubicin → porphyrin) was used to localize nanodox in the xenografts, and 690 nm light exposure to activate it. Such photo-nanotherapy was highly effective in reducing tumor volume. Histopathology and flow cytometry revealed CD4 + and CD8 + immune cell infiltration of xenografts. Overall, the ocular model shows potential for examining the relationships between neoplastic growth, neovascularization and other features of the immune microenvironment, and for evaluating treatment response longitudinally *in vivo*.

1. Introduction

Animal models are indispensable for understanding tumor biology and for drug development. Transplantable tumor models (syngeneic or xenograft) derived from tumor cell lines have been used for decades in cancer research [1]. Longitudinal, cellular level resolution *in vivo* imaging has become an increasingly desirable feature for animal models [2,3]. Thus, an ideal model should not only enable precise measurement of tumor development, but also quantification of nanotherapeutic delivery, tumor response to treatment and the tumor microenvironment, such as blood vessels, fibroblasts, immune cells, and extracellular matrix

#345121 https://doi.org/10.1364/BOE.10.000151
Journal © 2019 Received 6 Sep 2018; revised 9 Nov 2018; accepted 10 Nov 2018; published 11 Dec 2018

Biomedical Optics EXPRESS

[3]. The dorsal skin fold chamber (DSFC) model was developed over 70 years ago to facilitate optical study of implantable tumors and their microvasculature [4]. However, the DSFC has questionable biological relevance to tumors with origin in internal organs, and in particular in the brain. Alternatives include surgically implanted windows that allow intravital microscopy of cranium, brain, mammary gland, spinal cord, and abdominal organs [5–9]. While each of these models has advantages, they share the limitation that the optical window is invasive and potentially disruptive of the natural microenvironment.

Non-invasive imaging modalities such as positron emission tomography (PET), bioluminescence, dynamic susceptibility contrast-enhanced perfusion MRI, magnetic resonance spectroscopy imaging (MRSI), etc. have their own limitations for probing cancer-associated neovascularization development [10–15]. The major benefit of our technology is its high volumetric resolution, allowing reliable investigation of small tumors and monitoring of volumetric changes in the range of tens of nanoliters.

The eye possesses its own optical window and imaging optics, the cornea and crystalline lens, which enable non-invasive, cellular-level resolution *in vivo* imaging of the retina and its microvasculature in humans, in healthy and diseased states [16–18]. Ocular optical coherence tomography rapidly generates an intrinsically volumetric representation of the retinal layers and vasculature with a 3D resolution of a few micrometers [19,20], while scanning laser ophthalmoscopy provides confocal reflectance and fluorescence images with similar lateral, though poorer axial resolution [21]. Recently, these imaging modalities have been adapted to the much smaller optical system of the mouse eye, fusing their capabilities and the higher numerical aperture of the mouse eye with the powerful toolkits of mouse genetics and optogenetics, and allowing *in vivo* studies of mouse retinal structure and function in unprecedented detail [22,23]. Taking advantage of this fusion, in this investigation we developed the mouse eye as a non-surgical window for longitudinal *in vivo* optical investigation of a xenograft model of glioblastoma, employing mouse ocular imaging that combines simultaneous OCT and SLO [24–28]. Glioblastoma is an aggressive tumor with a high rate of recurrence. It is categorized as grade IV astrocytoma [29]. It is one of the most invasive, rapidly growing types of glial tumors, commonly spreading into nearby brain tissue effecting visual capabilities and spreading to the optic nerve [30]. By repeated *in vivo* imaging of individual xenografts over several months, the methodology provided quantitative tracking of tumor development, of the delivery of theranostic nanoparticles, and of tumor and tissue response to optically stimulated nanotherapeutic treatment [31].

2. Methods

2.1. Mouse husbandry

Animals were cared for and handled in accordance with National Institutes of Health Guidelines for the care and use of experimental animals and protocols approved by the Institutional Animal Care and Use Committee of the University of California, Davis. Nude (Nu/Nu) mice 6-8 weeks of age were obtained from Harlan (Livermore, CA), and maintained on a 12:12 light cycle.

2.2. Glioblastoma cell preparation and ocular transplantation

Human glioblastoma cells expressing GFP (U87MG-GFP) adherent to the bottom of a T75 flask were trypsinized with 0.05% trypsin-EDTA and neutralized with culture medium. Floating cells were collected and washed twice, resuspended in phosphate-buffered saline (PBS) at 10^7/ml, and maintained on ice for immediate ocular injection. Aliquots of the cells were routinely imaged with a Nikon A1 confocal microscope at 20X and 40X for quality control, including assessment of GFP fluorescence and cell size (diameter 10.3 ± 3.2 μm, mean ± s.d., 120 cells from 4 preparations). Ocular transplantation of cells between the retinal pigment epithelium (RPE) and the neural retina and was performed under visual guidance of a

Biomedical Optics EXPRESS

2-3X dissection microscope using the method of Matsumoto et al [32]. Mice were anesthetized with 1 to 4% isoflurane, and pupils dilated with 1% tropicamide and 2.5% phenylephrine. A small scleral incision was made in the superior limbus (12 o'clock) with the bevel of 31G needle (BD Ultra-Fine Short Needle), with superficial penetration to drain aqueous humor and reduce intraocular pressure. A 34G needle (Retinal Pigment Epithelium Kit, WPI, Sarasota, FL) connected to a 10 µl syringe (NanoFiL-100, WPI) was then passed through the incision and slowly inserted into the subretinal space so that the blunt needle tip was within 1 to 1.5 mm of the optic nerve head in the superior retina. A small volume (0.5 or 1.0 µL) of the cell suspension was gently injected under control of a microinjection pump (Nanoliter 2010 UMP3 controller, WPI) at a rate of 225-450 nL/s. The conjunctiva was repositioned with forceps, and a lubricant eye gel (GenTeal, Novartis, Switzerland) applied to the cornea. A coverslip was gently pressed to the cornea, and the fundus was evaluated with the microscope. Mice having retinal holes, or subretinal or vitreous hemorrhages were excluded from the study.

2.3. Treatment of xenograft glioblastoma with light-activated nanoparticles

After undergoing a prescribed period of growth (typically, once the tumors began an exponential growth phase) ocular xenograft glioblastomas were treated with light-stimulated nanoparticles, as described by Li et al. [31]. The ~20 nm micellar nanoparticles are composed of amphiphilic telodendrimers with a porphyrin-analogue component linked via polyethylene glycol and are loaded during self-assembly with doxorubicin. For treatment, the mouse was injected by tail vein with 100 µl of "nanodox" nanoparticles in PBS at a concentration of 1 mg/ml. One hour after the tail vein injection, the tumor region was irradiated locally in the ocular imaging apparatus with 690 nm light calibrated to deliver a total of 100 to 150 J cm^{-2} over a period of 15 to 30 min [31].

2.4. In vivo multimodal imaging

For retinal imaging, the mice were anesthetized with 2-4% isoflurane and their body temperature maintained by a heating pad (37°C) attached to micropositioner (Phoenix Research Labs, Pleasanton, CA) that allowed rotational and translational adjustment for alignment. The pupils were dilated with tropicamide and phenylephrine, and the corneal surface wetted with Gel Tears containing 0.2% carbomer (Chem-Pharm Fabrik, Berlin, DE. The Gel Tears also served to maintain a homogeneous refractive surface between the cornea and a custom 0 diopter contact lens (Unicon Corporation, Osaka, Japan).

The multimodal imaging apparatus comprises a SLO unit and an OCT unit, as previously described [31]. For the SLO sub-system a 488 nm laser (Coherent, 488-30FP, 200 µW at the pupil) served as the imaging light source, including excitation of nanoparticle FRET fluorescence (doxorubicin → porphyrin), while a 685 nm laser (Coherent, 685-40C, 1.2 mW) served for photoactivation of the PEG-porphyrin nanoparticles [31]. Reflected and fluorescence light from the retina were acquired by two PMTs (Hamamatsu, H7422-20, –40, respectively). The reflected/fluorescence light could be also directed to a spectrometer (Ocean Optics, QE65000) for spectral analysis. The OCT light source is a superluminescent diode light source with a 132 nm band centered on 860 nm, and delivers 600 µW at the plane of the mouse pupil. The diameter of the coaligned light beams at the pupil plane was ~0.5 mm, so that the beams passed into the eye with no vignetting through the 2.5 mm dilated mouse pupil. The OCT subsystem collects A-scans (single tomographic axial samples) at 100 kHz, with an axial resolution ~2 µm dictated by the source coherence length, while the SLO and OCT subsystems have x-, y- analogue resolutions of ~3.5 µm [33].

2.5. Image analysis and statistics

A standard OCT volume sampled a retinal area of 1.6 mm × 1.6 mm (assuming an angular conversion factor of 32 µm/deg) [33] and comprised 796 B-scans (horizontal scans), with

Biomedical Optics EXPRESS

each B-scan in turn comprising 2000 A-scans (axial backscatter profiles). Six spatially consecutive B-scans were averaged to reduce the speckle noise in the OCT images. Xenograft tissue was readily identifiable in OCT volume data by several criteria, including elevated scattering, abnormal layering, and spatial coincidence with SLO GFP fluorescence. Tumor thickness maps and volumes were extracted with semi-automated segmentation software [34,35]. From several B-scans of a clearly identified tumor region, the software was trained on 7 different gradient-based criteria, which were then applied automatically with subsequent curation to localize the full, 3D extent of the tumor within the larger OCT volume. Phase-variance analysis of the OCT volume data, which provides capillary-resolution OCT-angiography [36,37], was used to identify all blood vessels in the OCT volume, and in particular the neovascularization in the tumor subvolume. Custom software was used to overlay the GFP-fluorescence images obtained with SLO with *en face* presentations of the simultaneously acquired OCT data [33], confirming the accuracy of the segmentation and also helping to visualize various features of the data. Imaging of individual xenografts was performed weekly to bi-weekly for up to 5 months, until the eye's optics were distorted by the tumor or the eye exhibited external inflammation, or successful treatment was achieved. As xenografts were usually implanted in both eyes and tumors developed at different rates, the mice were routinely checked for signs of redness, discharge, or discomfort in both eyes. If an eye exhibited any of these signs, the campus veterinarian was contacted. If the condition was determined to be untreatable, the animal was euthanized by CO_2 inhalation, complying with UC Davis IACUC humane endpoints policy, and its eyes were collected for histology.

2.6. Immunohistochemistry

Mice were euthanized by CO_2 narcosis, and the eyes gently removed and fixed in 4% paraformaldehyde (PFA) in PBS for 5 min at room temperature. Anterior segments were then removed, the remaining eyecups fixed for another 20 minutes, and then dehydrated in 30% sucrose at 4°C overnight. The eyecups were embedded in OCT Compound (Tissue-Tek, Sakura, CA) and frozen at –20°C, then cryo-sectioned through the optic nerve at a thickness of 20 µm in the sagittal plane using a Micron HM 550 cryostat (Thermo-Fisher Scientific, Kalamazoo, MI). Chicken anti-GFP (1:100, 600-901-215, Rockland, Limerick, PA) was used to label glioblastoma cells, and rabbit polyclonal anti-collagen IV antibody (1:100, ab6586, Abcam, Cambridge, MA) to label blood vessels for assessing neovascularization, and rabbit anti-CD8A antibody (TA302180, Origene, Rockville, MD) to label lymphocyte infiltration. Alexa 488-conjugated goat anti-chicken and Alexa 633-conjugated goat anti-rabbit (both 1:200, Invitrogen Life Technologies) antibodies were used as secondaries. Cryosections were mounted with ProLong gold antifade reagent (Invitrogen Life Technologies), and imaged with a Nikon A1 confocal/multiphoton imaging system with a 40X water immersion objective as shown in Fig. 5.

2.7. Flow cytometry

CD4 + and CD8 + cells were isolated and quantified from the retina based on a slightly modified version of a method described previously [38]. In brief, the retinas and RPE-choroid complex from 2 eyes were separately collected and thoroughly minced with ophthalmic scissors in 1 ml of digestion mix containing 2 mg/ml Collagenase D, 28U/ml DNase I (both from Sigma-Aldrich, St. Louis, MO) in Hibernate medium (HBSS, Gibco, Thermo-Fisher Scientific, Carlsbad, CA). The tissue was digested at 37ºC in a water bath for 60 min, and re-suspended in 4 ml of Hibernate medium. The homogenate was filtered through a 140 µm mesh screen (Sigma-Aldrich) and centrifuged, and the supernatant carefully removed. Cell pellets were fixed in 1 ml of 4% PFA for 10 min at RT, then blocked and permeabilized for 15 min at RT in 200 µl of 1.5% BSA/0.5% Triton X-100. Brilliant violet 421 anti-mouse CD4 antibody (100437, 1:100, Biolegend, San Diego, USA) or APC anti-mouse CD8b antibody (126613, 1:100, Biolegend) was mixed with Alexa Fluor 488 anti-GFP antibody (338007,

Biomedical Optics EXPRESS

1:100, Biolegend), added into the cell solution and incubated overnight at 4ºC. Finally, the cell suspensions were washed and re-suspended in 300 µl PBS. Data were acquired on a BD LSRII flow cytometer (BD Biosciences, San Jose, CA): 10,000 events were collected for each tissue sample and analyzed with FlowJo software (Tree Star, LLC, Ashland, OR). Debris was eliminated by FSC-A vs. SSC-A gating prior to analysis.

3. Results

3.1 Simultaneous volumetric and fluorescence imaging of ocular xenografts

Xenografts were created by subretinal microinjection of freshly passed GFP+ human glioblastoma cells (U87MG-GFP) into mouse eyes (Fig. 1(A)). The location of the transplanted cells mimics that of most ocular metastases [39]. Eyes were imaged *in vivo* prior to the injection and periodically thereafter with simultaneous optical coherence tomography and confocal scanning laser ophthalmoscopy, enabling multiple features of the xenografts to be visualized and colocalized.

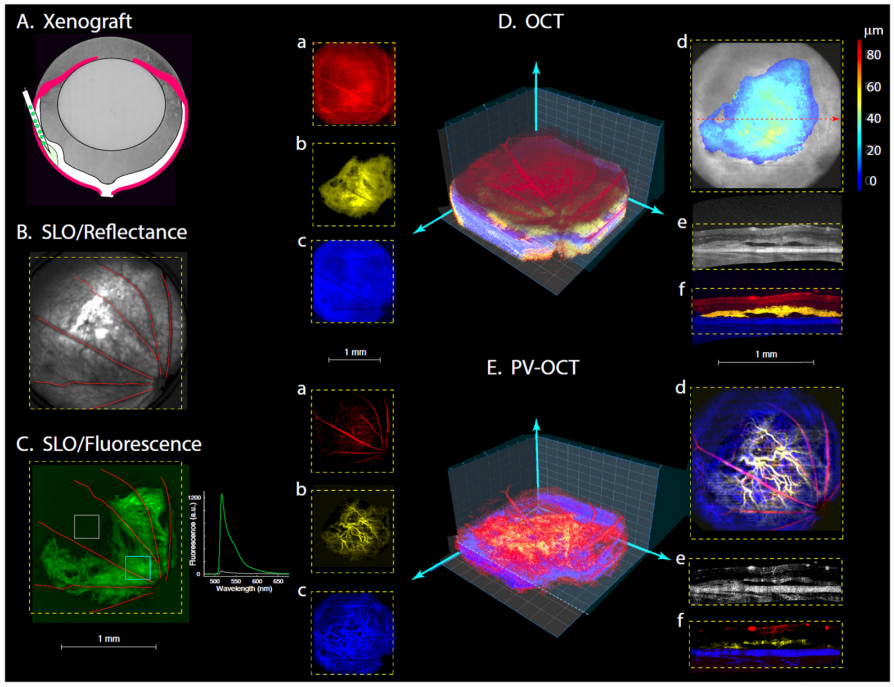

Fig. 1. Creation and characterization of ocular xenograft with simultaneous SLO (ex 488 nm) and OCT (860 nm) over wide retinal field (51 deg visual angle). A. Schematic illustrating subretinal transplantation of GFP+ glioblastoma cells. B-E. All panels are from the right eye of a nude mouse injected 104 days earlier with 5000 glioblastoma cells. B, C. SLO reflectance and fluorescence images. The optic nerve head is in the lower right corner of the images. Inset in C: GFP emission spectrum recorded from the two regions defined by the boxes superimposed on the fluorescence image. Da-f. OCT volumetric results. A 3D representation is shown (see also Visualization 1), along with *en face* presentations at left of the tumor (b, yellow), the retina anterior to the tumor (a, red) and posterior (c, blue; choroid, sclera). (In the central 3D representations z-axis grid lines are spaced 80 µm apart, while x-,y- grid lines are spaced by160 µm.) (d) *En face* view of the anterior retinal surface with the segmented tumor superimposed as a color-coded depth map. (e) and (f) B-scans (depth slices) taken at the position of red dashed arrow in (d); in (e) the strength of the OCT signal is presented in gray-scale, while in (f) the structures are color coded as in (a-c). Ea-f. OCT volumetric angiography: the same OCT data were analyzed for temporal phase-variance, which identifies voxels with red blood cell movement. The color coding of the panels corresponds to that used in E (see also Visualization 2). Note the tumor neovascularization in Eb, d, f.

Biomedical Optics EXPRESS

Real-time SLO reflectance imaging served as an orientation guide, allowing the experimenter to arrange the mouse so as to visualize a specific area of the retina, based on the map of the major blood vessels entering and exiting the optic disc (Fig. 1(B)). GFP-band SLO fluorescence imaging revealed the location of transplanted cells (Fig. 1(C)), and the specificity of the fluorescence as arising from GFP+ cells was confirmed by emission spectroscopy (1(C), inset). OCT was used to measure depth-resolved profiles of light scattering by the tissue, allowing volumetric mapping of the tumor morphology (Fig. 1(D)). The tumor region was readily identified and segmented in the OCT volumetric data by its abnormal layering and elevated scattering (Fig. 1(Db), (De), (Df); see also Visualization 1), as well as by colocalization of these distinctive OCT features with the GFP fluorescence (Fig. 1(C)). OCT-angiography (OCT-A), obtained from phase-variance post-processing [36], provided depth-resolved visualization of the vasculature (Fig. 1(E)), including that of the neovascularized tumor (Fig. 1(Eb), (Ed)).

3.2 Longitudinal imaging reveals three distinct growth patterns of xenograft tumors

Multimodal SLO and OCT imaging was used to study the xenografts of individual eyes in *vivo* over periods of up to several months (Fig. 2). SLO reflectance imaging of the superficial retinal vasculature provided a map for highly reliable session-to-session alignment, while the SLO GFP-band fluorescence images revealed changes in the glioblastoma cell population. The simultaneously recorded OCT data revealed corresponding changes in tumor volume (Fig. 2, "Thickness Map"; OCT B-scan) and in neovascularization (yellow, "Angiography").

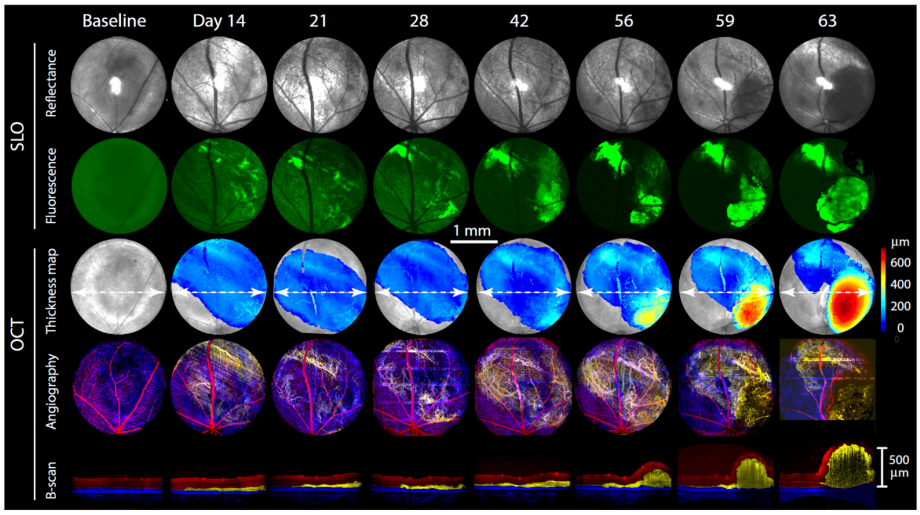

Fig. 2. Growth pattern of an ocular glioblastoma measured *in vivo* over a two-month period. The upper two rows of images present SLO reflectance and fluorescence images, while the bottom three rows present simultaneously acquired OCT results (see Fig. 1 for details of acquisition and analysis). The series of green SLO fluorescence images reveal the location of GFP+ cells (the baseline fluorescence image was contrast-enhanced to reveal the major blood vessels). The first row of OCT images presents a color-coded tumor thickness map overlaid on an *en face* image of the superficial retinal surface (gray). The second row presents a depth color-coded angiogram, with red corresponding to the normal superficial retinal vasculature, yellow the tumor vasculature, and blue the posterior (choroidal) vasculature (as in Fig. 1(E)). The lowermost row of images presents slices (B-scans) through the OCT volume data taken at the position of the white dashed lines overlaid on the thickness maps, with depth color coding corresponding to that used for the vasculature and serve to illustrate the disposition of the tumor in 3D, and its increasing volume. All images have the same length scale (center of figure).

Biomedical Optics EXPRESS

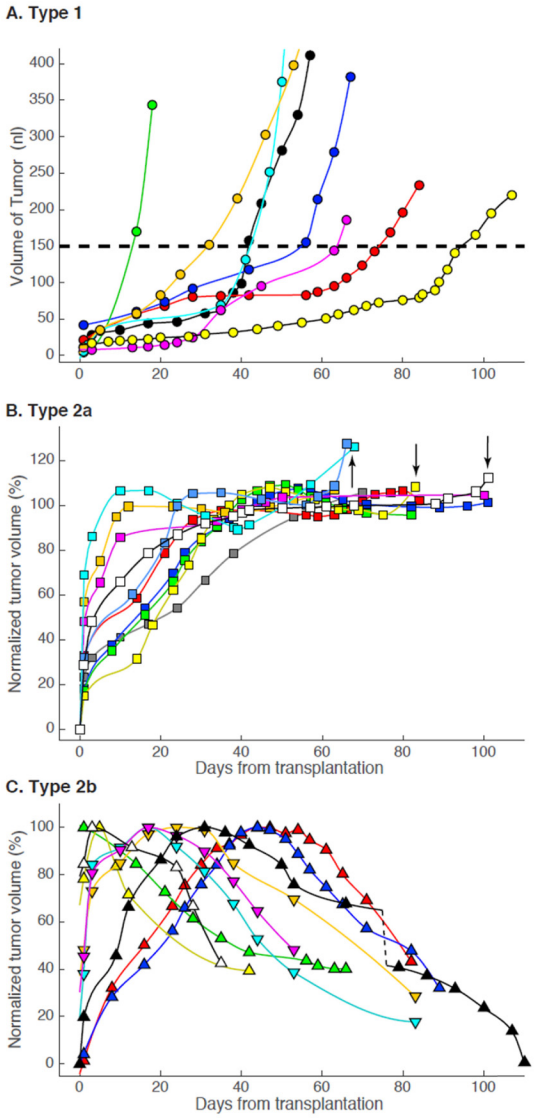

Fig. 3. Growth patterns of glioblastoma xenografts. A. Type 1: tumors whose volume exceeded 150 nL and that underwent highly accelerated growth (n = 8). The yellow filled symbols are from the tumor imaged in Fig. 1, while the dark blue filled symbols are from the tumor imaged in Fig. 2. A dashed line has been drawn at a volume of 150 nL; for comparison, the total volume of the retina from its vitreal surface to the posterior choroid in the 51 deg image field is between 5- and 10-fold greater. B. Type 2a: tumors that exhibited a plateau phase of growth (n = 10); arrows identify 4 growth patterns that appeared (post hoc) to be accelerating at the time the mouse was sacrificed. C. Type 2b: tumors that grew to a maximum volume and then underwent spontaneous decline (n = 9). Different colored symbols and lines are used for different tumors: each symbol represents the tumor volume derived (cf. Figs. 1, 2) from OCT measurements on the post-transplantation day indicated by the abscissa, while the smooth lines connecting the points are splines (the dashed black line in panel C represents a 20 day gap, which was omitted so that the lattermost time points of this xenograft would fit on a 110 day scale).

Changes induced by the xenograft were restricted to the area of the transplanted cells: thus, ocular tissue outside the region defined by GFP fluorescence exhibited normal retinal layering and vasculature. A regular feature of tumor progression seen in these images was an

Biomedical Optics EXPRESS

initial period (days 1- 28) of relative dormancy, followed by rapid neovascularization (day 42), and a correspondingly rapid tumor volume increase (days 56-63). The OCT data were processed to quantify tumor volumes, which are provided on the corresponding tumor thickness maps. The GFP fluorescence patterns and OCT tumor volumetrics provide complementary information; thus, the fluorescence provides unequivocal evidence for the presence of, and changes in the xenograft, while the OCT data provide information about tissue remodeling, including neovascularization.

A goal of this study was to test the efficacy of local treatment of ocular glioblastomas with light-activated nanoparticles [31]. Design of a treatment protocol required that xenograft growth be characterized in an untreated control group, so we applied the time-series protocol of Fig. 2 to a population of ocular xenografts. Based on their later phase of growth we classified tumors into three categories (Fig. 3). Type 1 tumors such as illustrated in Fig. 2 underwent exponential growth after a variable dormant period (Fig. 3(A)). Type 2 tumors grew to a maximum over a period about 40 days, followed either by a plateau (Type 2a; Fig. 3(B)) or by spontaneous decline (Type 2b, Fig. 3(C)). The Type 2a and Type 2b subpopulations were indistinguishable by initial growth trajectory, and the average plateau volume of Type 2a tumors (25 ± 7 nL, mean ± sem, n = 10) statistically indistinguishable from of the maximum volume of Type 2b tumors (28 ± 5 nL, n = 9). In addition, over the first 20 days the shallow growth phase for 7 of 8 of the Type 1 tumors had a volume of 35 ± 9 nL, only 40% larger than the average plateau volume of Type 2a's.

Despite the similarities in their initial growth phases, Type 2a and Type 2b xenografts were clearly distinguished by their behavior after reaching maximum growth. Thus, after reaching a plateau, Type 2a's never declined, and indeed, 4 of the 10 Type 2a tumors appeared poised to undergo more rapid growth (likely conversion to Type 1) at the time when the experiment was terminated (arrows in Fig. 3(B)). In contrast, all Type 2b xenografts underwent spontaneous decline soon after reaching a transient maximum. The mutual exclusivity of the Type 2a and Type 2b categories arises in part from a definition (plateau phase vs. decline). However, the absence of spontaneous decline in volume of any tumor that had a stable growth plateau lasting for at least 20 days, combined with the fact that some Type 2a's appeared to initiate a second growth phase, suggests that the distinction manifests an intrinsic difference in the tissue response to the xenograft.

3.3 Successful treatment of glioblastoma xenografts with light-stimulated nano-doxorubicin

We treated glioblastoma xenografts with light-activated nanoparticles ("nanodox"; [31]. Nanodox are 20 nm nanoparticles self-assembled from amphiphilic polyethylene glycol (PEG) telodendrimers with porphyrin in their shell and doxorubicin in the core (Fig. 4(A)). Light of 690 nm captured by porphyrin in the nanodox generates a triple therapeutic effect of heat, oxygen free radicals, and breakdown of the nanoparticles with release of doxorubicin [29]. An additional valuable feature of nanodox is that doxorubicin can serve as a FRET donor with porphyrin in the PEG shell acting as the acceptor. This feature was used to establish the presence of nanodox in xenografts (Fig. 4(B)): thus, while 488 nm excitation of the glioblastoma gave rise to an emission spectrum with a strong GFP signature (Fig. 4(B), upper panel), after tail vein injection of nanodox the deep red spectral region exhibited an unmistakable signature of porphyrin FRET emission (Fig. 4(B), lower panel, Days 35,45).

We treated tumors with nanodox following the protocol of Li et al. [31]. We began treatment of tumors 20 to 30 days after transplantation, at a time when growth was occurring in all but 11% of the control population (Fig. 3). For each treatment, one hour after tail vein injection of nanodox the tumor region as defined by GFP fluorescence was irradiated with 690 nm light calibrated to deliver 100 to 150 J cm^{-2} over a period of 15 to 30 min. We found that 3 such photo-nano treatments (as used by Li et al. [31]) were inadequate to stop the growth of Type 1 xenografts (Fig. 4(C)). We thus undertook a more aggressive approach,

Biomedical Optics EXPRESS

repeatedly treating another population of tumors of until volume decline was observed (Fig. 4(D)). All (13/13) of the repeatedly treated tumors declined in volume to ~50% or less of their maxima (Fig. 4(D)) and were on declining trajectories at the time the experiments were terminated. Nonetheless, the existence of the Type 2b controls raises the possibility that some of the treated tumors declined spontaneously rather than as a consequence of treatment. Because Type 2b's comprise only 33% (9/27) of the control population, only 4 = 0.33 x 13 of the treatment group would be expected to decline spontaneously. Stated more rigorously, assuming a binomial distribution with p = Pr(decline) = 0.33, the probability that all 13 tumors would spontaneously decline is $p^{13} = 5.5 \times 10^{-7}$, and so it can therefore be concluded that the nanodox treatment was highly effective.

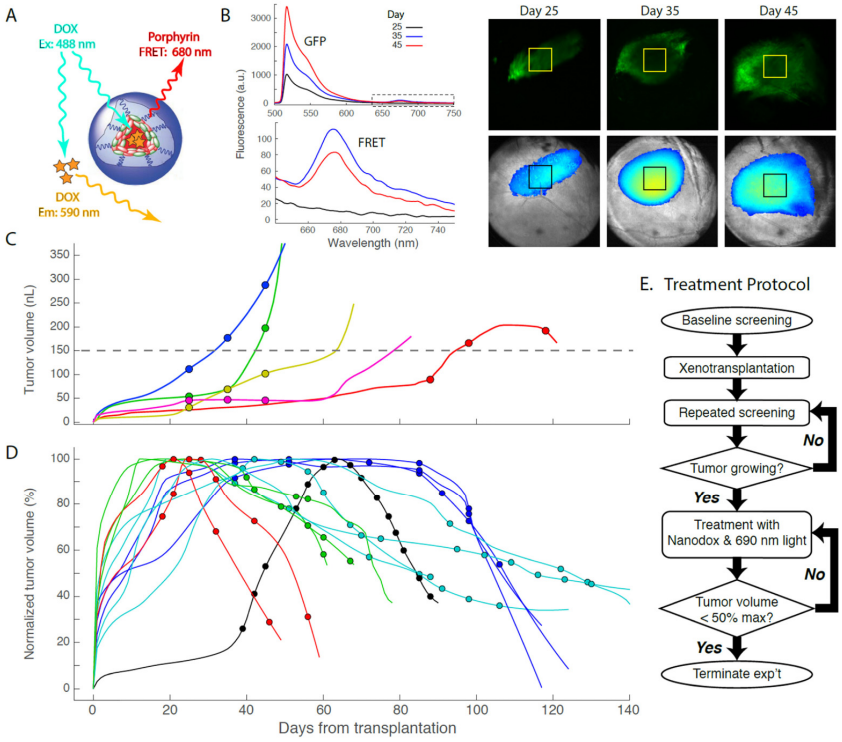

Fig. 4. Treatment of ocular glioblastomas with nanodoxorubicin. A. Schematic diagram of the 20 nm PEG-porphyrin nanoparticle loaded in its core with doxorubicin (see Li et al., 2010 for details). 488 nm light excites doxorubicin: in solution its emission peak is at 590 nm; confined in the nanodox particle, excited doxorubicin non-radiatively transfers energy to the porphyrin, which has a FRET emission peak at ~680 nm. B. Fluorescence emission (ex 488 nm) from a GFP+ glioblastoma on different days after the transplant (yellow squares on fluorescence images indicate regions from which the emission spectra were taken). The spectrum and image of day 25 were taken without nanodox, while those of days 35 and 45 were taken after tail-vein injection of nanodox. The strong GFP emission of the glioblastoma cells dominates the mid-spectral range, but a distinctive emission band peaking at 680 nm is present: lower plot ("FRET") shows the data in the dashed box of the upper plot on expanded scales. C. Limited (3X) treatment of Type 1 tumors with nanodox. Each symbol represents the tumor volume on the day of a treatment. D. Aggressive nanodox treatment of xenografts beginning around day 20 to 30 after transplantation. Treatment continued in each case until the tumor declined to ~50% of its maximal volume or less. The black filled symbols correspond to a Type 1 tumor (Fig. 3(A)) that reached a maximum volume of 420 nL. (In C, D tumor measurements are only plotted as symbols for the days of treatment; volume measurements from other days are not illustrated by discrete points, but rather presented by the continuous lines (splines), as in Fig. 3.). E. Treatment protocol illustrated in form of flow chart.

Biomedical Optics EXPRESS

Two additional facts support the conclusion that nanodox treatments were successful. First, 5 of the 13 tumors whose volume declined during the treatments transitioned through stable plateaus (Fig. 4(D), dark and light blue colored symbols and lines); in contrast, none of the 10 untreated tumors that exhibited plateaus in growth underwent spontaneous decline (Type 2a, Fig. 3(B)), and indeed 4 of 10 seemed poised for rapid growth. Second, one of the tumors that was successfully treated was clearly Type 1 (filled black symbols and black line). This tumor reached a maximum volume of 420 nL on day 63, but shrunk rapidly over the time course of treatment. In contrast, none of the 8 untreated control Type 1 tumors whose volume exceeded 150 nL declined in volume (Fig. 3(A)), and only 1 of the 5 Type 1 tumors given 3 treatments declined (Fig. 4(C)).

3.4 Histopathology of ocular xenograft glioblastomas

Histology of rodent eyes provides an efficient means of confirming and extending *in vivo* observation of xenograft tumors (Fig. 5). When the *in vivo* phase of the investigation of an ocular xenograft ended and the mouse was terminated, its eyes were enucleated, fixed and cryo-sectioned for *ex vivo* histochemistry. The tumor region was readily located in the cryosections (Fig. 5(A), (B)), and confocal microscopy used to confirm features observed with *in vivo* imaging, and to define additional features. Thus, for example, tumor neovascularization was confirmed with collagen IV staining, and usually revealed the blood vessels intrinsic to the tumor connected with the choroidal vasculature (Fig. 5(Aa)-(Ac)).

Also confirmed was the relatively circumscribed extent of the tumors and the normal status of the tissue away from the tumor: thus, completely normal retinal layering and vascularity is seen at distances of ~1 mm from the tumor (Fig. 5(Ac), (Bc)). An example of a feature not detectable with our current *in vivo* imaging toolkit was the presence in the tumors of cell surface markers CD8 (Fig. 5(Ba), (Bb)) and CD4 (not shown), which are co-receptors respectively for specific MHC I and MHC II T-cell receptors found on monocytes, macrophages, dendritic cells and helper T-cells.

3.5 Lymphocyte infiltration into tumors

As abundant CD8-immunostaining was observed in cryosections of the tumors in the athymic nude mice, we used flow cytometry to address the question of whether cytotoxic T-cells might be enhanced in xenografts (Fig. 6). Ocular tumors provided a valuable preparation for addressing this question, because ocular tissue can be efficiently isolated and prepared for flow cytometry, and moreover the untreated fellow eye provides a natural control for the eye with a xenograft. Thus, the untreated eye shares genetics and life history with the eye having the xenograft, and is matched with respect to tissue sample size. The flow cytometry data confirmed that no cells expressing GFP were detectable in the uninjected eye, and also revealed that the eye with the xenograft had highly reliable 3.5-fold and 41-fold increases in cells expressing CD4 and CD8 surface markers, respectively.

4. Discussion

In this investigation we have presented a novel mouse tumor model. It enables longitudinal, *in vivo* investigation of aspects of cancer biology including tumor growth dynamics (Figs. 2, 3), neovascularization inside tumor microenvironment (Figs. 1-2; 5-6), and treatment response to nanotherapeutics (Fig. 4). Transplanting as few as 500 human glioblastoma cells into the eye can initiate a readily detectable xenograft glioblastoma. Most xenografts exhibited a relatively quiescent phase that lasted for weeks to months, followed by a much more rapid growth phase (Fig. 3(A), (B)); however about 30% underwent spontaneous remission (Fig. 3(C)). Early and aggressive treatment with light-activated nanotherapeutics [31] completely reversed tumor growth (Fig. 4(D)). While three phototherapy treatments were usually ineffective when tumors had entered their rapid growth phase (Fig. 4(C)), extended treatment of even such

Biomedical Optics EXPRESS

rapidly growing tumors could successfully reverse tumor growth (Fig. 4(D), filled black circles).

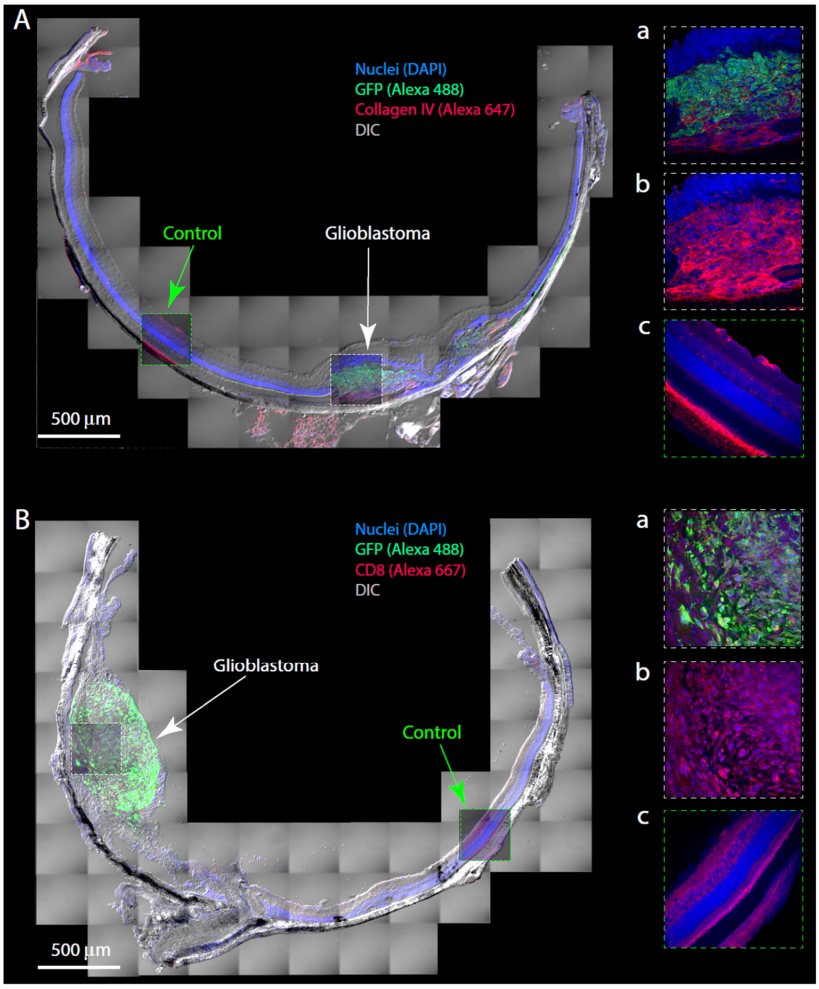

Fig. 5. Histology and histopathology of ocular xenografts. A, B. Montage of images of cryosections of eyes with glioblastoma xenografts, immuno-labeled to highlight features of the tumors, including GFP (expressed in the glioblastoma cells), vasculature (collagen IV), and MHC differentiation marker CD8. The panels at right are confocal slices from the center of the cryosection, immunolabeled as indicated on the figure; the same images are presented overlaid with 50% transparency on the montage. Aa, triply labeled portion of the tumor (DAPI, GFP, collagen IV); Ab, same confocal slice as Aa, but without the GFP immunolabel; Ac confocal slice from a control region where no tumor cells were present, labeled as Ab. Aa-Ac serve to illustrate the tumor neovascularization and its interconnection with the choroidal vasculature, and also the pattern of collagen IV labeling of normal retinal (superior) and choroidal (posterior) vasculature. Ba, triply labeled portion of the tumor (DAPI, GFP, CD8); Bb, same confocal slice as Ba, but with the GFP labeling removed; Bc, control region illustrating normal pattern of CD8 labeling. The Type 1 tumor of panel A was created with the injection of 10,000 cells in 1 µL, and the animal sacrificed 13 weeks after injection; growth data from this tumor are also shown in Fig. 3(A), filled dark blue symbols. The Type 1 tumor of panel B was created by the injection of 5000 cells in 0.5 µL, and the mouse sacrificed 10 weeks after injection. Its initial growth trajectory is shown in Fig. 3(A) (filled black circles); the tumor was treated with light-activated nanodox, and the treatment series illustrated in Fig. 4(D) (filled black symbols).

Biomedical Optics EXPRESS

In addition to the advantages afforded by non-invasive *in vivo* imaging, the ocular tumor model also provides benefits for efficient post-mortem examination. The latter includes histology of tumor microenvironmental features (Fig. 5) and flow cytometry analysis of tissue changes induced by the tumor such as immune cell infiltration (Fig. 6).

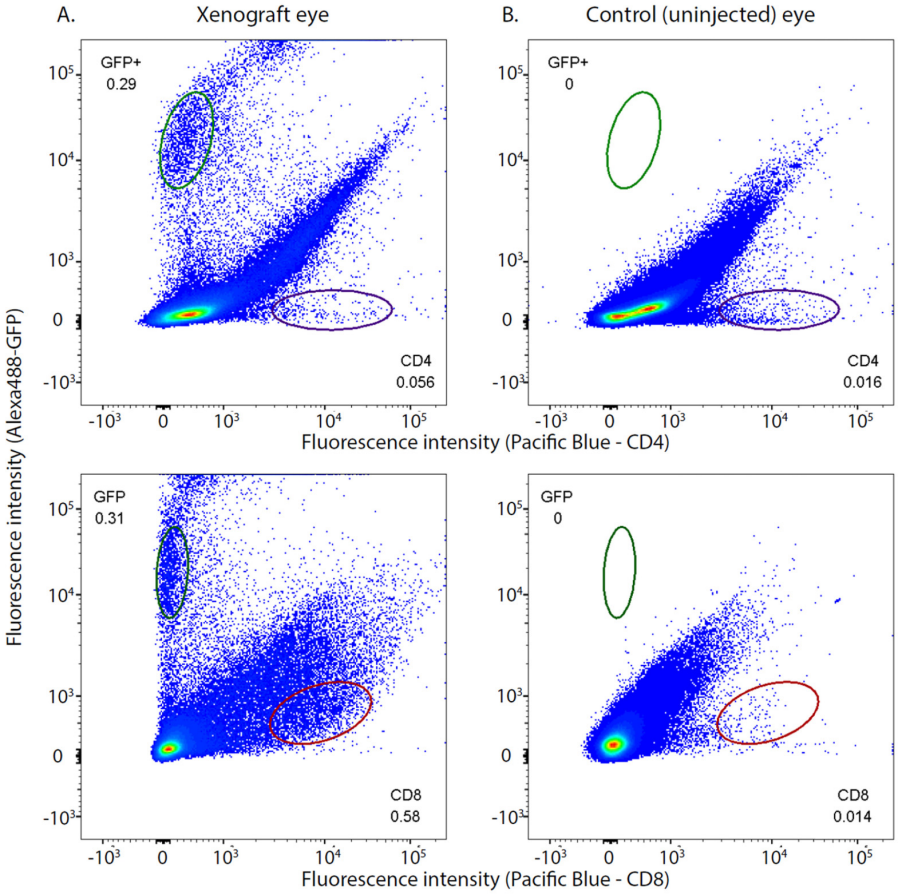

Fig. 6. Flow cytometry of cells from an eye with a xenograft glioblastoma reveals a tumor-associated increase in cells expressing CD8 epitope. In all four panels the ordinate gives the fluorescence intensity of cells labeled with an anti-GFP antibody tagged with Alexa 488 dye, while the abscissa is the fluorescence intensity of cells labeled with antibodies to CD4 (upper row of panels) or CD8 (lower row) conjugated to Pacific Blue dye. The left column of panels was obtained with cells from the eye that had a glioblastoma xenograft, while the right column of panels was obtained with exactly the same gating parameters from the cells identically harvested from the control (uninjected) eye of the same nude mouse. Counts in the plot regions indicated by the ellipses were used for statistical analysis. There were no GFP+ counts in the cells from the uninjected eye. The eye with the xenograft had statistically reliable 3.5-fold and 41-fold increases in cells expressing CD4 and CD8 cell surface markers, respectively, relative to the control eye. The flow cytometry data were analyzed with FloJoTM software and the numbers on the panels represent the fractions of the total count in the elliptical regions. The Type 1 tumor was generated by injection of 500 cells; the corresponding growth curve is illustrated in Fig. 3A by filled orange circles. This experiment was replicated in a second mouse with similar results.

4.1 Immune cell infiltration into tumors

Our results show that even in athymic (Nu/Nu) mice, cells expressing CD4 and CD8 markers infiltrate xenograft tumors (Figs. 5, 6). In this context it is notable that in xenografts that underwent spontaneous remission (Type 2b; Fig. 3(C)) as well as those treated extensively

Biomedical Optics EXPRESS

with nanodox (Fig. 4(D)), not only did the GFP+ cells disappear, but also the associated prior tissue volume increase measured with OCT. These finding implicate an active tissue remodeling process, and suggest the hypothesis that cytotoxic CD8 + lymphocytes contributed to the spontaneous tumor remission observed in some xenografts (Type 2b; Fig. 3(C)) and to remodeling after therapeutic destruction of tumor tissue. Future experiments employing syngeneic tumor variants and mouse lines with constitutively labeled monocytes [40,41] will be needed to address these issues.

4.2 Treatment of xenograft glioblastomas with nano-doxorubicin

We have previously demonstrated that nanoporphyrin loaded with doxorubicin is a highly effective nanophototherapeutic agent against xenograft and transgenic breast cancer models [31]. The intraocular tumor model reported here allows us to visualize the intratumoral distribution of the nanotherapeutics, and in the case of nanodox, the light-activated breakdown of the nanocarrier and release of doxorubicin. In addition, the imaging system also enables us to focus the laser beam (690 nm) directly on the tumor (100 to 150 J cm^{-2} over a period of 15 to 30 min) for photodynamic and photothermal therapy, without irradiating non-tumor tissue (Fig. 5). We found that three photo-treatments were inadequate to control the tumor (Fig. 4(C)). However, additional repeated photo-treatments did shrink all treated tumors (Fig. 4(D)). We believe the efficacy of phototherapy will be further improved by finding the optimum time interval between intravenous injection of nanodox and light irradiation, i.e., the time when nanodox has maximally cumulated at tumor sites. Previous work with non-therapeutic PEG nanoparticles suggests the optimum interval will be between 1 and 24 hrs, as most of nanoparticles are cleared from the vasculature by 24 hrs after intravenous injection [31].

4.3 Validity as the ocular cancer model for investigating central nervous system cancer

The retina of the eye is part of the central nervous system, and thanks to its optical system is a readily "approachable part of the brain" [42]. The neural retina develops from optic vesicles of the nascent forebrain of the neural tube, and ultimately derives from neuroepithelial stem cells in the same manner as other central nervous system (CNS) neurons and glial cells. A major issue in CNS cancer therapeutics is drug delivery across the blood brain barrier (BBB) [43,44], which is formed by tight and adherens junctions of vascular endothelial cells, with further contributions from pericytes and perivascular glial cell processes. The blood retinal barrier (BRB) of the anterior retinal vasculature is thought to be identical to that of the BBB. Nonetheless, the portion of the BRB formed by the tight junctions of the retinal pigment epithelial (RPE) cell layer – whose apical side faces the neural retina and whose basal side apposes the fenestrated choriocapillaris and adjacent choroid vasculature – appears to distinguish the BRB from the BBB. The RPE component of the BRB, however, is not a distinguishing feature when compared to the homologous CNS structure, the choroid plexus of the brain's ventricular system. Specifically, the choroid plexus comprises a layer of epithelial cells whose apical side faces the brain's neural parenchyma and whose basal side faces the fenestrated capillary bed of the plexus. Moreover, the choroid plexus is a major route for BBB exchange of many compounds from the vasculature to the brain [45]. Thus, from the broadest perspective the BRB and BBB are fully parallel. The surgical technique used here transplants cancer cells between the two barriers of the BRB (Fig. 1(De), (Df)) and the tumors develop within the neural parenchyma. We conclude that ocular xenografts provide an excellent model not only for the investigation of many aspects of CNS tumor biology, but also for the delivery of nanotherapeutics across the BBB/BRB and across the blood tumor barrier (BTB).

Biomedical Optics EXPRESS

5. Concluding remarks

While primary human ocular cancers such as retinoblastoma and ocular melanoma are relatively rare, the number of clinical ocular metastases is ~20,000 cases/year in the US [46], such that many individuals with primary lung or breast tumors first present with ocular symptoms [47,48]. Thus, in addition to its many values for investigation of basic mechanisms of CNS cancer and nanotherapeutics, the ocular xenograft is a clinically relevant model for investigation of metastatic lesions.

We are developing the ocular tumor model for use with patient-derived xenografts and also with syngeneic cancer cell lines such as B16 melanoma in normal mice. Syngeneic ocular models, when used in conjunction with fluorescently labeled immune cells [40,41], should enable cellular-level resolution monitoring of check-point immunotherapy *in vivo*, and a similar approach may be used with NSG mice humanized with fluorescently labeled immune cells [49,50]. Many fluorescent protein-based tumor cell lines capable of reporting specific cell signaling responses have been used successfully to study tumor biology and the cell signal response to targeted therapy [51]. We envision that ocular xenografts derived from these cells lines will allow visualization of biochemical and morphological changes in developing tumors and their responses to particular targeted therapies.

Funding

NCI U01 CA198880, R01 EY026556, R01 CA199668, R01 HD086195 and UC Davis Comprehensive Cancer Center; UC Davis Small Animal Ocular Imaging NEI Core (5P30 EY012576).

Disclosures

The authors declare that there are no conflicts of interest related to this article.

References

1. M. Saxena and G. Christofori, "Rebuilding cancer metastasis in the mouse," Mol. Oncol. **7**(2), 283–296 (2013).
2. C.-P. Day, G. Merlino, and T. Van Dyke, "Preclinical mouse cancer models: a maze of opportunities and challenges," Cell **163**(1), 39–53 (2015).
3. B. A. Teicher, ed., *Tumor Models in Cancer Research* (Springer Science & Business Media, 2010).
4. G. E. Koehl, A. Gaumann, and E. K. Geissler, "Intravital microscopy of tumor angiogenesis and regression in the dorsal skin fold chamber: mechanistic insights and preclinical testing of therapeutic strategies," Clin. Exp. Metastasis **26**(4), 329–344 (2009).
5. R. P. Barretto, T. H. Ko, J. C. Jung, T. J. Wang, G. Capps, A. C. Waters, Y. Ziv, A. Attardo, L. Recht, and M. J. Schnitzer, "Time-lapse imaging of disease progression in deep brain areas using fluorescence microendoscopy," Nat. Med. **17**(2), 223–228 (2011).
6. L. Ritsma, E. J. Steller, E Beerling, C.J. Loomans, A. Zomer, C Gerlach, et al., "Intravital microscopy through an abdominal imaging window reveals a pre-micrometastasis stage during liver metastasis," Sci Transl Med **4**(158), 158ra145 (2012).
7. L. Ritsma, E. J. A. Steller, S. I. J. Ellenbroek, O. Kranenburg, I. H. M. Borel Rinkes, and J. van Rheenen, "Surgical implantation of an abdominal imaging window for intravital microscopy," Nat. Protoc. **8**(3), 583–594 (2013).
8. D. Kedrin, B. Gligorijevic, J. Wyckoff, V. V. Verkhusha, J. Condeelis, J. E. Segall, and J. van Rheenen, "Intravital imaging of metastatic behavior through a mammary imaging window," Nat. Methods **5**(12), 1019–1021 (2008).
9. C. Ricard, F. Stanchi, G. Rougon, and F. Debarbieux, "An orthotopic glioblastoma mouse model maintaining brain parenchymal physical constraints and suitable for intravital two-photon microscopy," J. Vis. Exp. **86**, 86 (2014).
10. L. García-Rojas, G. Adame-Ocampo, G. Mendoza-Vázquez, E. Alexánderson, and J. L. Tovilla-Canales, "Orbital positron emission tomography/computed tomography (PET/CT) imaging findings in Graves ophthalmopathy," BMC Res. Notes **6**(1), 353 (2013).
11. E. Salmon, C. Bernard Ir, and R. Hustinx, "Pitfalls and Limitations of PET/CT in Brain Imaging," Semin. Nucl. Med. **45**(6), 541–551 (2015).
12. R. Muzaffar, M. A. Shousha, L. Sarajlic, and M. M. Osman, "Ophthalmologic abnormalities on FDG-PET/CT: a pictorial essay," Cancer Imaging **13**(1), 100–112 (2013).

Biomedical Optics EXPRESS

13. J. Miyamoto, K. Tatsuzawa, K. Owada, T. Kawabe, H. Sasajima, and K. Mineura, "Usefulness and Limitations of Fluorine-18-Fluorodeoxyglucose Positron Emission Tomography for the Detection of Malignancy of Orbital Tumors," Neurol. Med. Chir. (Tokyo) **48**(11), 495–499 (2008).
14. M. B. Gutowski, L. Wilson, R. N. Van Gelder, and K. L. Pepple, "In Vivo Bioluminescence Imaging for Longitudinal Monitoring of Inflammation in Animal Models of Uveitis," Invest. Ophthalmol. Vis. Sci. **58**(3), 1521–1528 (2017).
15. F. W. van Leeuwen, J. C. Hardwick, and A. R. van Erkel, "Luminescence-based Imaging Approaches in the Field of Interventional Molecular Imaging," Radiology **276**(1), 12–29 (2015).
16. S. Mo, B. Krawitz, E. Efstathiadis, L. Geyman, R. Weitz, T. Y. Chui, J. Carroll, A. Dubra, and R. B. Rosen, "Imaging Foveal Microvasculature: Optical Coherence Tomography Angiography Versus Adaptive Optics Scanning Light Ophthalmoscope Fluorescein Angiography," Invest. Ophthalmol. Vis. Sci. **57**(9), OCT130 (2016).
17. J. Lee and R. Rosen, "Optical Coherence Tomography Angiography in Diabetes," Curr. Diab. Rep. **16**(12), 123 (2016).
18. D. R. Williams, "Imaging single cells in the living retina," Vision Res. **51**(13), 1379–1396 (2011).
19. D. Huang, E. A. Swanson, C. P. Lin, J. S. Schuman, W. G. Stinson, W. Chang, M. R. Hee, T. Flotte, K. Gregory, C. A. Puliafito, and et, "Optical coherence tomography," Science **254**(5035), 1178–1181 (1991).
20. W. Drexler and J. G. Fujimoto, "State-of-the-art retinal optical coherence tomography," Prog. Retin. Eye Res. **27**(1), 45–88 (2008).
21. P. F. Sharp, A. Manivannan, H. Xu, and J. V. Forrester, "The scanning laser ophthalmoscope--a review of its role in bioscience and medicine," Phys. Med. Biol. **49**(7), 1085–1096 (2004).
22. P. Zhang, A. Zam, Y. Jian, X. Wang, Y. Li, K. S. Lam, M. E. Burns, M. V. Sarunic, E. N. Pugh, Jr., and R. J. Zawadzki, "In vivo wide-field multispectral scanning laser ophthalmoscopy-optical coherence tomography mouse retinal imager: longitudinal imaging of ganglion cells, microglia, and Müller glia, and mapping of the mouse retinal and choroidal vasculature," J. Biomed. Opt. **20**(12), 126005 (2015).
23. R. J. Zawadzki, P. Zhang, A. Zam, E. B. Miller, M. Goswami, X. Wang, R. S. Jonnal, S. H. Lee, D. Y. Kim, J. G. Flannery, J. S. Werner, M. E. Burns, and E. N. Pugh, Jr., "Adaptive-optics SLO imaging combined with widefield OCT and SLO enables precise 3D localization of fluorescent cells in the mouse retina," Biomed. Opt. Express **6**(6), 2191–2210 (2015).
24. E. S. Levine, A. Zam, P. Zhang, A. Pechko, X. Wang, P. FitzGerald, E. N. Pugh, Jr., R. J. Zawadzki, and M. E. Burns, "Rapid light-induced activation of retinal microglia in mice lacking Arrestin-1," Vision Res. **102**, 71–79 (2014).
25. Y. Jian, J. Xu, M. A. Gradowski, S. Bonora, R. J. Zawadzki, and M. V. Sarunic, "Wavefront sensorless adaptive optics optical coherence tomography for in vivo retinal imaging in mice," Biomed. Opt. Express **5**(2), 547–559 (2014).
26. D. M. Schwartz, J. Fingler, D. Y. Kim, R. J. Zawadzki, L. S. Morse, S. S. Park, S. E. Fraser, and J. S. Werner, "Phase-variance optical coherence tomography: a technique for noninvasive angiography," Ophthalmology **121**(1), 180–187 (2014).
27. A. Z. Zam, E. N. Pugh Jr, and R. J. Zawadzki, "Evaluation of OCT for quantitative in vivo measurements of changes in neural tissue scattering in longitudinal studies of retinal degeneration in mice," Proc. SPIE **8934**, 893422 (2014).
28. P. Z. Zhang, E. N. Pugh, Jr, and R. J. Zawadzki, "Evaluation of state-of-the-art imaging systems for in vivo monitoring of retinal structure in mice: current capabilities and limitations," Proc. SPIE **8930**, 893005 (2014).
29. T. L. Chiu, M. J. Wang, and C. C. Su, "The treatment of glioblastoma multiforme through activation of microglia and TRAIL induced by rAAV2-mediated IL-12 in a syngeneic rat model," J. Biomed. Sci. **19**(1), 45 (2012).
30. A. M. Meleis, A. Mahtabfar, S. Danish, and R. A. Foty, "Dexamethasone-mediated inhibition of Glioblastoma neurosphere dispersal in an ex vivo organotypic neural assay," PLoS One **12**(10), e0186483 (2017).
31. Y. Li, T. Y. Lin, Y. Luo, Q. Liu, W. Xiao, W. Guo, D. Lac, H. Zhang, C. Feng, S. Wachsmann-Hogiu, J. H. Walton, S. R. Cherry, D. J. Rowland, D. Kukis, C. Pan, and K. S. Lam, "A smart and versatile theranostic nanomedicine platform based on nanoporphyrin," Nat. Commun. **5**(1), 4712 (2014).
32. H. Matsumoto, J. W. Miller, and D. G. Vavvas, "Retinal detachment model in rodents by subretinal injection of sodium hyaluronate," J. Vis. Exp. **79**, 50660 (2013).
33. P. Zhang, A. Zam, Y. Jian, X. Wang, Y. Li, K. S. Lam, et al., "In vivo wide-field multispectral SLO-OCT mouse retinal imager: longitudinal imaging of ganglion cells, microglia, and Muller glia, and mapping of the mouse choroidal vasculature," J. Biomed. Opt. **20**(12), 126005 (2015).
34. R. J. Zawadzki, A. R. Fuller, D. F. Wiley, B. Hamann, S. S. Choi, and J. S. Werner, "Adaptation of a support vector machine algorithm for segmentation and visualization of retinal structures in volumetric optical coherence tomography data sets," J. Biomed. Opt. **12**(4), 041206 (2007).
35. A. Fuller, R. Zawadzki, S. Choi, D. Wiley, J. Werner, and B. Hamann, "Segmentation of three-dimensional retinal image data," IEEE Trans. Vis. Comput. Graph. **13**(6), 1719–1726 (2007).
36. D. Y. Kim, J. Fingler, J. S. Werner, D. M. Schwartz, S. E. Fraser, and R. J. Zawadzki, "In vivo volumetric imaging of human retinal circulation with phase-variance optical coherence tomography," Biomed. Opt. Express **2**(6), 1504–1513 (2011).

Biomedical Optics EXPRESS

37. D. Y. Kim, J. Fingler, R. J. Zawadzki, S. S. Park, L. S. Morse, D. M. Schwartz, S. E. Fraser, and J. S. Werner, "Optical imaging of the chorioretinal vasculature in the living human eye," Proc. Natl. Acad. Sci. U.S.A. **110**(35), 14354–14359 (2013).
38. L. Legroux, C. L. Pittet, D. Beauseigle, G. Deblois, A. Prat, and N. Arbour, "An optimized method to process mouse CNS to simultaneously analyze neural cells and leukocytes by flow cytometry," J. Neurosci. Methods **247**, 23–31 (2015).
39. R. C. Eagle, Jr., "The pathology of ocular cancer," Eye (Lond.) **27**(2), 128–136 (2013).
40. N. Saederup, A. E. Cardona, K. Croft, M. Mizutani, A. C. Cotleur, C. L. Tsou, R. M. Ransohoff, and I. F. Charo, "Selective chemokine receptor usage by central nervous system myeloid cells in CCR2-red fluorescent protein knock-in mice," PLoS One **5**(10), e13693 (2010).
41. A. J. Iqbal, E. McNeill, T. S. Kapellos, D. Regan-Komito, S. Norman, S. Burd, N. Smart, D. E. Machemer, E. Stylianou, H. McShane, K. M. Channon, A. Chawla, and D. R. Greaves, "Human CD68 promoter GFP transgenic mice allow analysis of monocyte to macrophage differentiation in vivo," Blood **124**(15), e33–e44 (2014).
42. J. E. Dowling, "The retina: an approachable part of the brain," (Harvard University Press, 1987), p 282.
43. M. J. Ochocinska, B. V. Zlokovic, P. C. Searson, A. T. Crowder, R. P. Kraig, J. Y. Ljubimova, T. G. Mainprize, W. A. Banks, R. Q. Warren, A. Kindzelski, W. Timmer, and C. H. Liu, "NIH workshop report on the trans-agency blood-brain interface workshop 2016: exploring key challenges and opportunities associated with the blood, brain and their interface," Fluids Barriers CNS **14**(1), 12 (2017).
44. N. Shonka, V. A. Venur, and M. S. Ahluwalia, "Targeted Treatment of Brain Metastases," Curr. Neurol. Neurosci. Rep. **17**(4), 37 (2017).
45. J. K. Laterra, L. A. Betz, and G. W. Goldstein, *"Blood—Cerebrospinal Fluid Barrier,"* in: G. J. Siegel, B. W. Agranoff, R. W. Albers, et al., editors. Basic Neurochemistry: Molecular, Cellular and Medical Aspects. 6th edition. (Philadelphia: Lippincott-Raven 1999)
46. V. M. L. Cohen, "Ocular metastases," Eye (Lond.) **27**(2), 137–141 (2013).
47. H. Demirci, C. L. Shields, A. N. Chao, and J. A. Shields, "Uveal metastasis from breast cancer in 264 patients," Am. J. Ophthalmol. **136**(2), 264–271 (2003).
48. S. U. Shah, A. Mashayekhi, C. L. Shields, H. S. Walia, G. B. Hubbard 3rd, J. Zhang, and J. A. Shields, "Uveal metastasis from lung cancer: clinical features, treatment, and outcome in 194 patients," Ophthalmology **121**(1), 352–357 (2014).
49. J. J. Morton, G. Bird, Y. Refaeli, and A. Jimeno, "Humanized Mouse Xenograft Models: Narrowing the Tumor-Microenvironment Gap," Cancer Res. **76**(21), 6153–6158 (2016).
50. T. Ashizawa, A. Iizuka, C. Nonomura, R. Kondou, C. Maeda, H. Miyata, T. Sugino, K. Mitsuya, N. Hayashi, Y. Nakasu, K. Maruyama, K. Yamaguchi, I. Katano, M. Ito, and Y. Akiyama, "Antitumor Effect of Programmed Death-1 (PD-1) Blockade in Humanized the NOG-MHC Double Knockout Mouse," Clin. Cancer Res. **23**(1), 149–158 (2017).
51. B. Sparta, M. Pargett, M. Minguet, K. Distor, G. Bell, and J. G. Albeck, "Receptor Level Mechanisms Are Required for Epidermal Growth Factor (EGF)-stimulated Extracellular Signal-regulated Kinase (ERK) Activity Pulses," J. Biol. Chem. **290**(41), 24784–24792 (2015).